ADVANCED FUNCTIONAL MATERIALS
www.afm-journal.de

Biodegradable Polyanhydrides as Encapsulation Layers for Transient Electronics

Yeon Sik Choi, Jahyun Koo, Young Joong Lee, Geumbee Lee, Raudel Avila, Hanze Ying, Jonathan Reeder, Leonhard Hambitzer, Kyungtaek Im, Jungwon Kim, Kyung-Mi Lee, Jianjun Cheng, Yonggang Huang, Seung-Kyun Kang, and John A. Rogers**

Bioresorbable electronic systems represent an emerging class of technology of interest due to their ability to dissolve, chemically degrade, disintegrate, and/or otherwise physically disappear harmlessly in biological environments, as the basis for temporary implants that avoid the need for secondary surgical extraction procedures. Polyanhydride-based polymers can serve as hydrophobic encapsulation layers for such systems, as a subset of the broader field of transient electronics, where biodegradation eventually occurs by chain scission. Systematic experimental studies that involve immersion in phosphate-buffered saline solution at various pH values and/or temperatures demonstrate that dissolution occurs through a surface erosion mechanism, with little swelling. The mechanical properties of this polymer are well suited for use in soft, flexible devices, where integration can occur through a mold-based photopolymerization technique. Studies of the dependence of the polymer properties on monomer compositions and the rates of permeation on coating thicknesses reveal some of the underlying effects. Simple demonstrations illustrate the ability to sustain operation of underlying biodegradable electronic systems for durations between a few hours to a week during complete immersion in aqueous solutions that approximate physiological conditions. Systematic chemical, physical, and in vivo biological studies in animal models reveal no signs of toxicity or other adverse biological responses.

1. Introduction

Bioresorbable electronic devices, as the basis for temporary implants that naturally resorb/dissolve in biofluids, provide the ultimate solution to problems of infection, hematogenous spread, and immune-mediated pathological tissue reactions caused by the presence and migration of conventional, permanent implants[1–4] and by the risks associated with secondary removal surgeries.[5,6] Recent literature highlights the broad range of capabilities that are now available with such technologies, as a subset of a more general class of system known as transient electronics: including circuits, radios, and power supply systems for physical sensors of pressure,[7] temperature, flow rate, motion,[8] and chemical species,[8,9] as well as photonic devices,[10] electrical stimulators,[11] thermal actuators,[8] and controlled drug-delivery vehicles[12,13] for use in areas of the body ranging from the intracranial space, to the abdominal cavity, to intramuscular regions of the lower extremity, to subdermal implantation at the dorsolateral area.[8,14]

Dr. Y. S. Choi, Dr. J. Koo, Y. J. Lee, Dr. G. Lee, Dr. J. Reeder, L. Hambitzer
Center for Bio-Integrated Electronics
Department of Materials Science and Engineering
Northwestern University
Evanston, IL 60208, USA

Prof. J. Koo
School of Biomedical Engineering
Korea University
Seoul 02841, Republic of Korea

R. Avila
Department of Mechanical Engineering
Northwestern University
Evanston, IL 60208, USA

H. Ying, Prof. J. Cheng
Department of Materials Science and Engineering
University of Illinois at Urbana-Champaign
Urbana, IL 61801, USA

The ORCID identification number(s) for the author(s) of this article can be found under https://doi.org/10.1002/adfm.202000941.

DOI: 10.1002/adfm.202000941

Dr. K. Im, J. Kim, Prof. K.-M. Lee
Global Research Laboratory
Department of Biochemistry and Molecular Biology
Korea University College of Medicine
Seoul 02841, Republic of Korea

Prof. Y. Huang
Center for Bio-Integrated Electronics
Department of Civil and Environmental Engineering
Mechanical Engineering
Materials Science and Engineering
Northwestern University
Evanston, IL 60208, USA

Prof. S.-K. Kang
Department of Materials Science and Engineering, Research Institute of Advanced Materials, Institute of Engineering Research
Seoul National University
Seoul 08826, Republic of Korea
E-mail: kskg7227@snu.ac.kr

Although carefully selected materials and component designs can yield bioresorbable devices with performance comparable to conventional, permanent analogues, extending the timeframes for their functional, stable operation beyond a few days can be difficult due to the intrinsic water-soluble nature of the constituent materials.[8–16] The most useful strategy to extend the operational lifetime is through the use of passive encapsulation layers[14,16,17] that serve as bioresorbable barriers to prevent interactions of biofluids with underlying active materials. For example, biodegradable inorganic materials formed by chemical or physical vapor deposition, such as silicon oxide, silicon nitride, and various metal oxides, in principle, can serve as water barriers due to their dense, close-packed atomic/molecule structure and their slow chemistry of degradation by hydrolysis.[15,16] Practical challenges, however, arise from their mechanical rigidity, their fragility and resulting difficulties in use with soft and time-dynamic biological tissues.[18] Layers of biodegradable polymers such as polylactic acid (PLA), poly(lactic-*co*-glycolic acid) (PLGA), and silk fibroin formed by spin-casting bypass some of these challenges, but their hydrophilic nature leads to levels of water permeability that are insufficient to serve as barriers to biofluds.[19] Furthermore, swelling of these hydrophilic polymers by water absorption can lead to deformations of the device platforms and, in some cases, fracture of the active electronic materials.

Here, we demonstrate the characteristics of a bioresorbable polyanhydride-based polymer with chemistry that leads to an intrinsic hydrophobic character. The resulting dissolution in water occurs through a surface erosion mechanism, with very little swelling, as required for use as an encapsulation layer for bioresorbable electronics. The mechanical properties support robust operation in flexible devices, and a mold-based photopolymerization technique facilitates processing and integration. Control over the monomer composition and the thickness provides routes to robust water-barrier characteristics for timescales that range from a few hours to a week. Systematic chemical, physical, and in vivo biological studies reveal all of the key characteristics of this polymer.

2. Results and Discussions

2.1. Synthesis of Polyanhydride

Figure S1 (Supporting Information) summarizes the synthesis of the polyanhydride, polybuthanedithiol 1,3,5-triallyl-1,3,5-triazine-2,4,6(1H,3H,5H)-trione pentenoic anhydride (PBTPA). 1,3,5-Triallyl-1,3,5-triazine-2,4,6(1H,3H,5H)-trione (TTT) provides multi-armed divinyl linkers, and both allyl containing monomers, 4-pentenoic anhydride (4PA) and TTT, can be cross-linked with 1,4-butanedithiol (BDT) through thiol–ene reactions initiated by exposure to ultraviolet (UV) light. **Figure 1**a illustrates the process for forming well-controlled films of this material using a mold-based photopolymerization technique. Here, a liquid mixture of the three chemical precursors (4PA, TTT, and BDT) and the photoinitiator infiltrates by capillary action through an inlet to an outlet of a mold of polydimethylsiloxane (PDMS) with surfaces treated with a self-assembled monolayer (SAM) of trichloro(1H, 1H, 2H, 2H-perfluorooctyl) silane. Passing UV light (intensity of 590 μW cm^{-2}; wavelength of 365 nm) for 5 min through the transparent PDMS photocures the liquid into a solid film of PBTPA with thicknesses (between a few to a few hundred micrometers, with variable profiles) and lateral dimensions defined by the geometry of the mold. This thiol–ene photopolymerization supports fast (<10 min) cross-linking without the need for organic solvents. The films of PBTPA show excellent mechanical stability under various deformations. As an illustration, photographs of films with uniform thicknesses of 300 μm during stretching (left), twisting (middle), and rolling (right) appear in Figure 1b.

Systematic studies of polymers formed with different ratios of the starting materials define the dependence of the hydrolysis kinetics, water absorption, water permeation, and mechanical properties on the polymer chemistry. The ratio of 4PA, TTT, and BDT can vary as long as the molar ratio of the alkene groups in 4PA and TTT, and the thiol functional group of BDT remain the same. Due to this stoichiometric relation, the relative ratio of 4PA and TTT sets the concentration of BDT. The hydrophobicity of PBTPA can be controlled through this ratio because 4PA contains the hydrophilic and degradable bond, while BDT provides the hydrophobic chain. Measurements focus on PBTPA films with three different ratios of 4PA, TTT, and BDT: 1:1:2.5, 1:2:4, and 1:4:7, respectively, as shown in Figure S2 (Supporting Information). Figure S3 (Supporting Information) shows Fourier-transform infrared (FTIR) spectroscopy spectra of PBTPA films with ratios of 1:1:2.5 (black), 1:2:4 (red), and 1:4:7 (blue). All three spectra reveal anhydride peaks at 1813 and 1744 cm^{-1}. The relative peak intensity of PBTPA 1:1:2.5 (black) is much higher than that of PBTPA 1:4:7 (blue), indicating a much higher ratio of anhydride group in PBTPA 1:1:2.5. Films with ratios of 1:1:2.5, 1:2:4, and 1:4:7 exhibit water contact angles of 68.4°, 71.8°, and 89.1°, respectively (Figure 1c and Table S1, Supporting Information). The results demonstrate that the relative ratio of BDT significantly affects the hydrophobicity of the material.

2.2. Degradation Behavior of PBTPA Immersed in Biofluid

In general, bioresorbable polyanhydrides undergo surface erosion in aqueous solutions because the rate of hydrolytic degradation at the surface is much faster than that of water diffusion into the bulk. The hydrolysis here refers to chain scission processes due to the hydrolytically labile anhydride bonds.[20,21] As illustrated in Figure S1 (Supporting Information), the degradation of PBTPA also occurs with

Prof. J. A. Rogers
Center for Bio-Integrated Electronics
Department of Materials Science and Engineering
Biomedical Engineering
Chemistry
Mechanical Engineering
Electrical Engineering and Computer Science
and Neurological Surgery
Simpson Querrey Institute for Nano/biotechnology
McCormick School of Engineering and Feinberg School of Medicine
Northwestern University
Evanston, IL 60208, USA
E-mail: jrogers@northwestern.edu

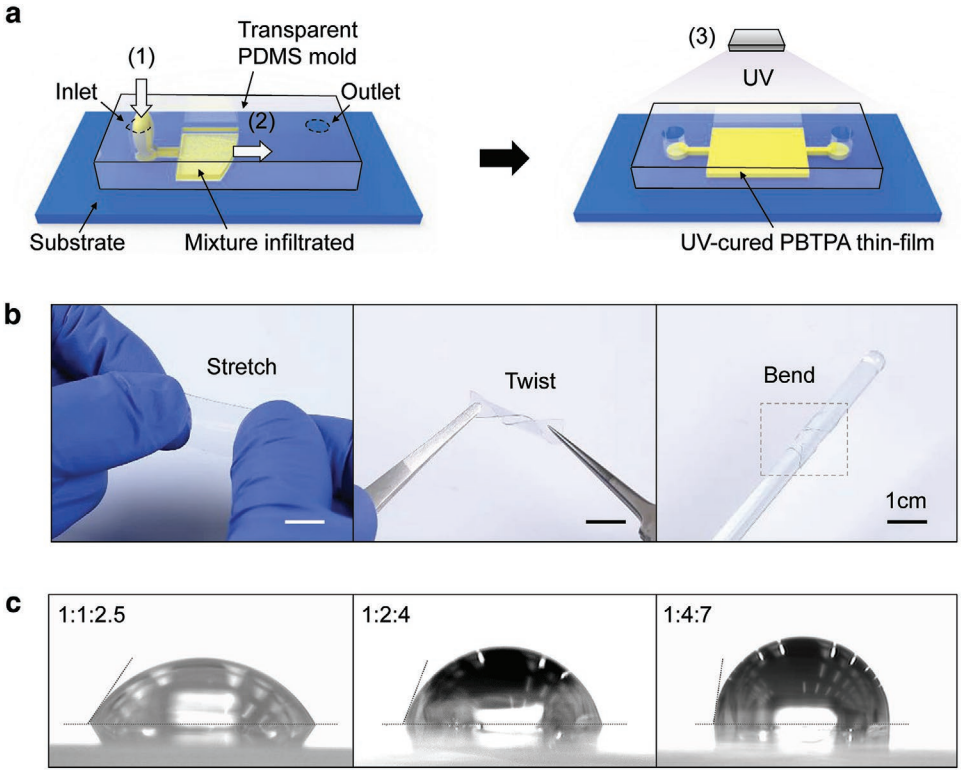

Figure 1. a) Method for fabricating films of PBTPAs: 1) Deliver a mixture of the three chemical precursors and photoinitiator into the inlet of a removable PDMS mold structure placed against a flat substrate. 2) Allow capillary forces to fill the solution into the reservoir defined by a relief structure in the mold. 3) Cure the material into a solid form by exposure to UV light (590 μW cm^{-2}, λ = 365 nm for 10 min). Removing the mold completes the process. The mold defines the shape and thickness of the PBTPA film. b) Image of a stretched (left), twisted (middle), and bent (right) film of PBTPA. The bending demonstration involves lamination onto a glass rod (ϕ = 5 mm). c) Representative photographs for the contact angle of water on the PBTPAs with three different ratios of 4PA, TTT, and BDT: 1:1:2.5, 1:2:4, and 1:4:7, respectively.

breakage of the anhydride bonds into two carboxylic acid bonds.[22]

Figure 2a summarizes the degradation behavior of PBTPAs in terms of change in weight as a function of time in aqueous solutions at various pH at room temperature (23 °C). The degradation of PBTPA 1:1:2.5 and PBTPA 1:4:7 occur most quickly and most slowly, respectively, at all pH values. At neutral conditions (pH 7.4; 23 °C) for the first 16 d, the hydrolysis rate of PBTPA 1:1:2.5 (≈1.14 × 10^{-3} g d^{-1}) is ≈27 times higher than that of PBTPA 1:4:7 (≈4.25 × 10^{-5} g d^{-1}), consistent with expectation based on the relative anhydride content. At acidic conditions (pH 5.7; 23 °C) for the first 6 d, the rate of hydrolysis of both PBTPA 1:1:2.5 (≈4.10 × 10^{-4} g d^{-1}) and PBTPA 1:4:7 (≈6.67 × 10^{-5} g d^{-1}) are much slower than those at neutral conditions. Since PBTPA degrades into carboxylic acids, solubilities of these byproducts increase with the concentration of OH^{-} ions. At low pH, the ability to solubilize is limited because the byproducts are in their unionized form. As a result, PBTPA degrades more slowly in acidic media than in basic media.[20,22,23]

The dissolution rate also depends on by temperature (Figure 2b). In phosphate buffered saline (PBS; pH 7.4), the dissolution rate of PBTPA 1:1:2.5 for the first 7 d at 60 °C (≈5.74 × 10^{-3} g d^{-1}) is ≈12 times higher than that at 23 °C (≈4.96 × 10^{-4} g d^{-1}) because the reaction rate of hydrophilic and degradable 4PA domains increases as temperature increases. In contrast, the dissolution rate of PBTPA 1:4:7 at all temperatures is relatively very low (<≈1.20 × 10^{-4} g d^{-1} at 60 °C) due to the hydrophobic chemistry of BDT, as designed. Images of PBTPA pieces after soaking in PBS (pH 7.4; at 23 °C) for 16 d show a similar trend (Figure S4, Supporting Information). Initially transparent samples (Figure S2, Supporting Information) turn white and opaque (Figure S4, Supporting Information) due to the hydrolysis of degradable groups, while PBTPA 1:4:7 remains transparent, consistent with its relatively low rate of dissolution. The dissolution rate for PBTPA 1:4:7 (PBS; pH 7.4) at physiological temperature (37 °C) can be calculated using the Arrhenius equation

$$k_{\mathrm{PBTPA}} = k_0 \cdot \exp(-E_{\mathrm{A}}/RT) \quad (1)$$

where k_0 is the pre-exponential factor, E_{A} is the activation energy, R is the universal gas constant (= 8.314 J K^{-1} mol^{-1}), and T is the absolute temperature. The measured dissolution rates of the PBTPA 1:4:7 at different temperatures yield values of k_0 and E_{A} as 1.14 × 10^{7} and 51 500 J mol^{-1}, respectively (Figure S5, Supporting Information), such that the dissolution rate is projected as ≈2.4 × 10^{-5} g d^{-1} at 37 °C for PBTPA 1:4:7. The rate of dissolution observed in this case implies that a PBTPA 1:4:7 with mass of 1 mg will completely dissolve within ≈42 d under this condition (pH 7.4; 37 °C). Figure S6 (Supporting

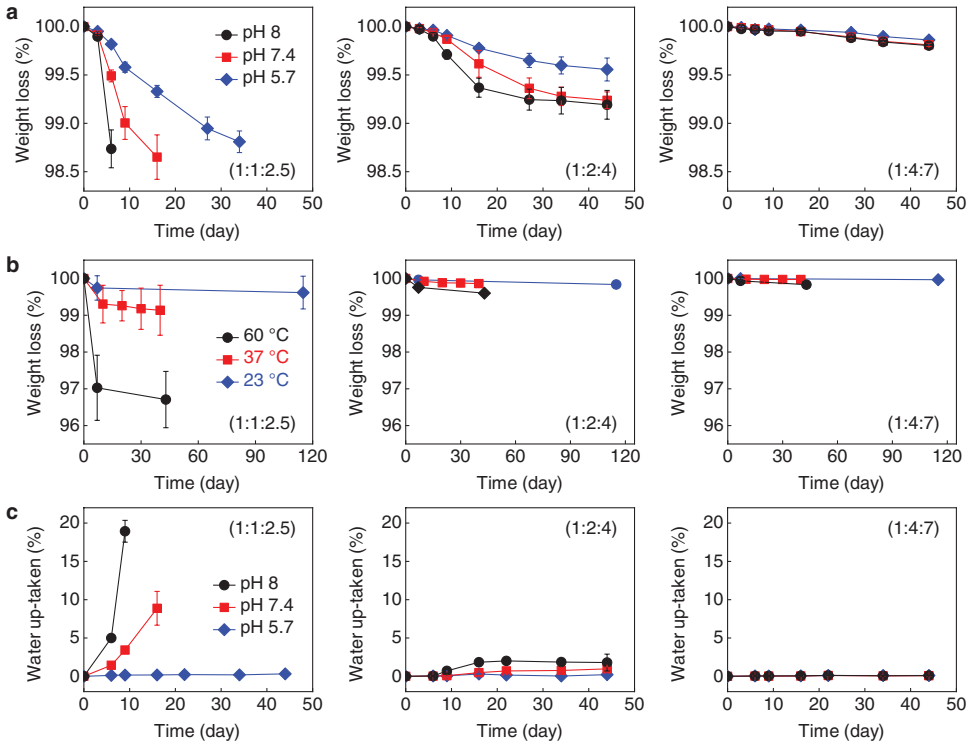

Figure 2. Hydrolysis kinetics and water absorption of three different PBTPA formulations in aqueous solutions at different pH values and temperatures. Insets are magnified plots. a) Degradation kinetics of three PBTPAs with three different compositions of 4PA, TTT, and BDT (left, 1:1:2.5; middle, 1:2:4; right, 1:4:7) in 0.1 M phosphate buffered saline (PBS) at three different pH values (black, pH 8; red, pH 7.4; blue, pH 5.7) at room temperature (23 °C). b) Degradation kinetics of three PBTPAs (left, 1:1:2.5; middle, 1:2:4; right, 1:4:7) in PBS (pH 7.4) at different temperatures (black, 60 °C; red, 37 °C; blue, 23 °C). c) The water absorption behavior of PBTPAs (left, 1:1:2.5; middle, 1:2:4; right, 1:4:7) on the pH value (black, pH 8; red, pH 7.4; blue, pH 5.7), as measured at room temperature. (a, right) Reproduced with permission from the Supporting Information.[8]

Information) highlights the changes in thickness of PBTPA 1:4:7 in PBS (pH 7.4) at physiological temperature (37 °C), over 15 d. The linear and continuous decrease (≈1.3 μm d^{-1}) in thickness is consistent with a surface erosion reaction mechanism, without a significant contribution of reactive diffusion.

The water absorption properties of PBTPA films in aqueous solutions at various pH at room temperature (23 °C) have relationships to the swelling characteristics (Figure 2c). At neutral conditions (pH 7.4; 23 °C), the water uptake is most significant in PBTPA 1:1:2.5, showing over 5% water absorption of their original sample weight after 16 d. The swelling of PBTPA 1:1:2.5 likely results from its high content of hydrophilic constituent (4PA). In contrast, within experimental uncertainties, PBTPA 1:4:7 does not undergo water uptake. The lack of swelling with PBTPA 1:4:7 likely follows from its high content of hydrophobic BDT. For both PBTPA 1:1:2.5 and PBTPA 1:2:4, the rate of water uptake at pH 8 (≈2.8×10^{-2} and ≈1.5×10^{-3} g d^{-1}, respectively) is much higher than at pH 5.7 (≈2.4×10^{-4} g d^{-1} for both PBTPAs), consistent with the relatively high rate of dissolution in basic media. Images of samples of PBTPA 1:1:2.5 immersed in solutions at three different pH values for 6 d support the result (Figure S7, Supporting Information). The sample at pH 8 swells and deforms significantly with complete loss of mechanical integrity after 6 d. In this case, the hydrophilic 4PA enhances water absorption and bulk erosion. Similar changes also occur at 16 and 35 d for pH 7.4 and 5.7, respectively. By contrast, PBTPA 1:4:7 shows no measurable dependence of water absorption on pH due to the hydrophobic chemistry.

2.3. Mechanical Properties and Thermal Behavior of PBTPA

Mechanical properties are important to consider for integration with soft tissues, whose Young's moduli (E) range from 100 Pa to 10 MPa,[24] and whose dynamic behaviors can involve repeated displacements of hundreds of micrometers at 1 Hz in the heart or brain,[25] volumetric changes up to 8% in the heart,[26] or large flexion and angular displacements in the skin and spinal cord.[27] **Figure 3**a shows the results of measurement of stress–strain responses of PBTPAs with different ratios of 4PA, TTT, and BDT. The tests use standard tensile specimens (ASTM-D1708; Figure S8, Supporting Information) with four samples (n = 4) per group, evaluated at a crosshead speed of 3 mm min^{-1} (MTS Sintech. 20G, USA). The ultimate tensile strength (UTS) of PBTPA 1:1:2.5, 1:2:4, and 1:4:7 are 0.40, 0.92, and 1.32 ± 0.11 MPa, respectively. The elongation at break of PBTPA 1:1:2.5, 1:2:4, and 1:4:7 are 32.7%, 27.5%, and 28.4 ± 6.7%, respectively. Figure 3b summarizes Young's modulus of these materials; PBTPA 1:1:2.5, 1:2:4, and 1:4:7 are 5.2, 17.9, and 25.1 ± 0.4 MPa, respectively. These results imply that the polymer elasticity of PBTPA can be adjusted to meet requirements of the target application by varying the ratio of

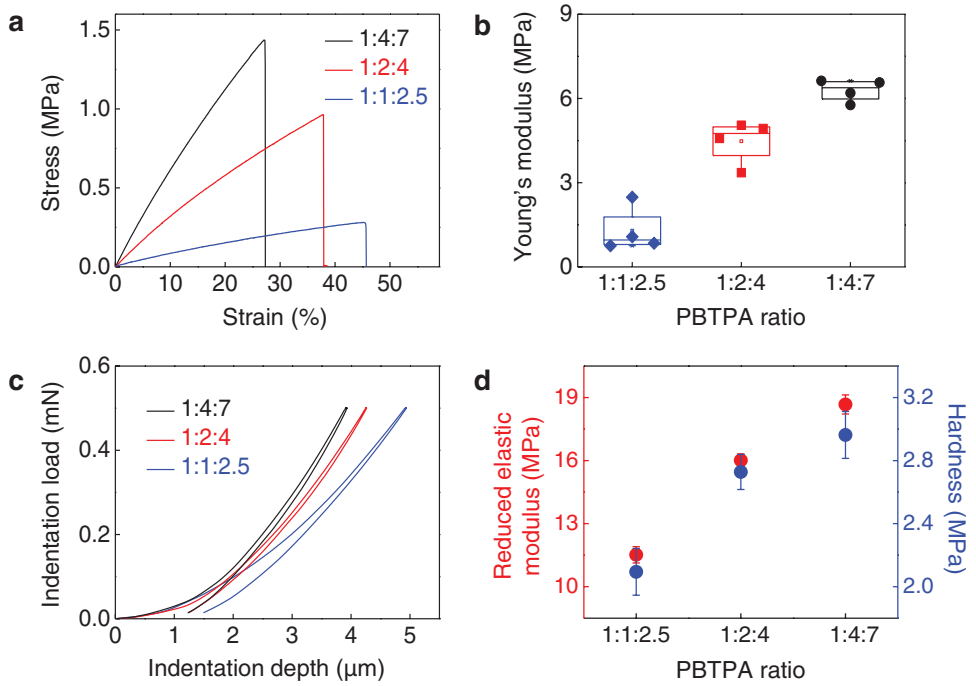

Figure 3. Characterization of the mechanical properties of various PBTPA formulations by nanoindentation and tensile test. a) Stress–strain curve of PBTPAs (black, 1:1:2.5; red, 1:2:4; blue, 1:4:7). b) Young's modulus of PBTPAs (black, 1:1:2.5; red, 1:2:4; blue, 1:4:7). c) Indentation load and depth response of PBTPAs with three different compositions of 4PA, TTT, and BDT (black, 1:1:2.5; red, 1:2:4; blue, 1:4:7). The large ratio of maximum indentation depth to final indentation depth is consistent with a strong elastic recovery. d) Reduced elastic modulus (red) and hardness (blue) of three different PBTPAs.

chemical constituents. The mechanical properties of commonly used biodegradable polymers are summarized in Table S2 (Supporting Information). Figure S9 (Supporting Information) shows the results of cyclical strain/stress measurements to maximum strains of 15%. All specimens with three different ratios show negligible plastic deformation (<0.7%).

The hardness is another mechanical property of interest. Data from nanoindentation tests on films of PBTPAs (≈130 μm) appear in Figure 3c as load–depth curves for forces of up to 500 μN (Berkovich indenter). The relatively large recovery of the indentation depth (>≈70% of maximum indentation depth) during unloading suggests that PBTPAs undergo primarily elastic deformations under these compressive forces. PBTPAs with higher TTT content show a smaller maximum indentation depth at the same applied load, implying that they are more rigid. Figure 3d shows the reduced elastic modulus and hardness extracted from these data. The reduced elastic modulus, defined as

$$\frac{1}{E^*} = \frac{1-\nu^2}{E} + \frac{1-\nu'^2}{E'} \tag{2}$$

where E^* is the reduced modulus, E is Young's modulus of tested material, ν is the Poisson's ratio of tested material, E' is Young's modulus of the conical indenter, and ν' is Young's modulus of the conical indenter. PBTPA 1:4:7 has the largest reduced elastic modulus and hardness, while PBTPA 1:1:2.5 shows the smallest values (the ranges of reduced elastic modulus and hardness are 11 to 18 MPa and 2 to 3 MPa, respectively).

Figure S10 (Supporting Information) provides results from thermogravimetric analysis (TGA) of PBTPA 1:1:2.5, 1:2:4, and 1:4:7. No measurable change in mass occurs until the thermal degradation temperature (T_d) of 350 °C, representing the compatibility of PBTPA of high temperature (<350 °C) device fabrication processes.

2.4. Water Permeability of PBTPA as an Encapsulation Layer for Bioelectronics

Impermeability to water is a key characteristic in the chemical design of substrates and encapsulation layers for bioresorbable electronics because these materials typically determine the time of stable operation.[14,16,17] Gradual hydrolysis of serpentine thin-film traces of Mg (length 21.35 mm, width 150 μm, thickness ≈300 nm) can be used to define the relative water permeability of encapsulation layers cast on top. A description of the test setup and the resistance changes of a Mg resistor without polymer encapsulation appears in Figures S11 and S12 (Supporting Information), respectively. We selected PLGA as a reference biodegradable polymer to provide context for the water permeability of PBTPA since PLGA is one of the most widely used biodegradable polymers for various biomedical applications, including transient electronics.[7–11] The water vapor permeability (WVP) of PLGA and other commonly used biodegradable polymers are summarized along with their key mechanical characteristics in Table S2 (Supporting Information). **Figure 4**a and Figure S13 (Supporting Information)

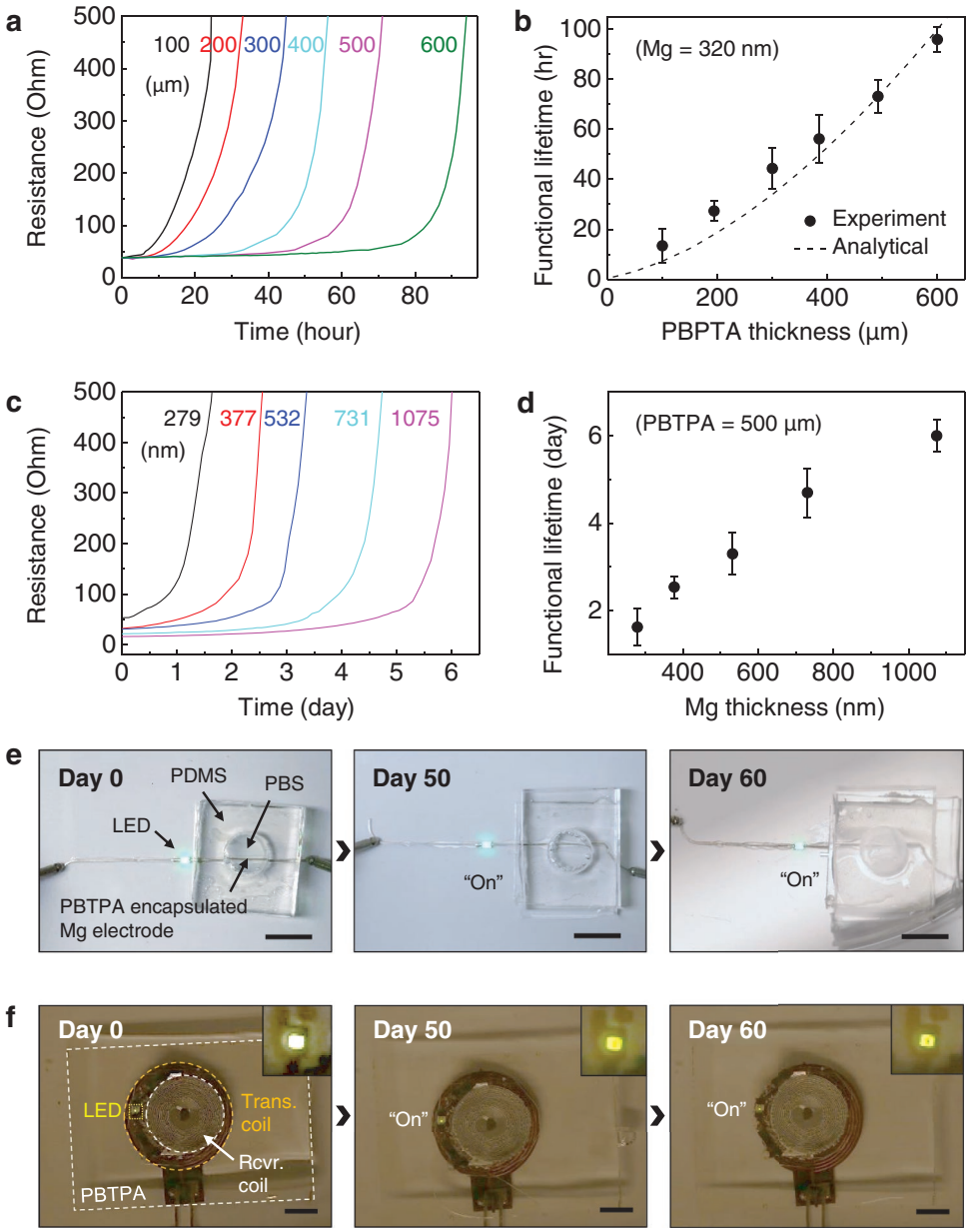

Figure 4. Water permeability tests of PBTPA encapsulation layers, in isolation and as used in simple wired and wireless devices. a) Measurements of changes in resistance of Mg traces (≈320 nm thick) encapsulated with PBTPA 1:4:7 while immersed in PBS (pH 7.4) at physiological temperature (37 °C). Various thicknesses of PBPTA 1:4:7 encapsulation were used: 100 μm (black), 200 μm (red), 300 μm (blue), 400 μm (cyan), 500 μm (magenta), 600 μm (olive). b) Measured functional lifetime (i.e., stable operation time), corresponding to the time over which the resistance remains finite, as a function of the thickness of the PBTPA 1:4:7 encapsulation layer. c) Measurements of changes in resistance of Mg traces encapsulated with PBTPA 1:4:7 (≈500 μm thick) while immersed in biofluids (PBS; pH 7.4) at physiological temperature (37 °C). Various thickness of Mg traces were used: 279 nm (black), 377 nm (red), 532 nm (blue), 731 nm (cyan), 1075 nm (magenta). d) Measured functional lifetime as a function of thickness of Mg traces. Mg traces are encapsulated by PBTPA 1:4:7 with thickness of ≈500 μm. e) Light-emitting diode (LED) that connects with a laser-cut strip of Mg (width, 300 μm; thickness, 50 μm) for testing the water-barrier properties of PBTPA 1:4:7 encapsulation (≈500 μm) by top-down diffusion. The series of images illustrates the change in intensity of the LED during various stages of immersion in PBS (pH 7.4) at physiological temperature (37 °C). Scale bar indicates 5 mm. f) Fully encapsulated, wireless powered LED system for testing the water-barrier properties of PBTPA 1:4:7 encapsulation on the top and bottom (1 mm). Besides the LED, all parts of the system use biodegradable materials (Figure S15, Supporting Information). The encapsulated devices are immersed in PBS (pH 7.4) at physiological temperature (37 °C) and operated wirelessly using a transmission coil placed underneath the glass reservoir. The insets show magnified views of the LED during operation. Scale bar indicates 5 mm.

show the time-dependent changes in the resistance of Mg traces encapsulated with various thicknesses of PBTPA 1:4:7 and PLGA (65:35 (lactide:glycolide), M_w 40–75 K), respectively, after immersion in PBS (pH 7.4; 37 °C). PLGA absorbs water quickly, such that water passes through to dissolve the Mg within 1–4 h (Figure S13, Supporting Information). The hydrophilicity of the ester bonds and the linear polymer structures in PLGA contribute to these behaviors.

By contrast, encapsulation with the most hydrophobic PBTPA 1:4:7 (600 μm) yields no change in electrical properties over 80 h (Figure 4a). Figure S14 (Supporting Information) shows a series of images corresponding to the dissolution of a Mg trace encapsulated with various thicknesses of PBTPA 1:4:7 after immersion in PBS (pH 7.4) for 46 h at 37 °C. Here, dissolution of Mg occurs throughout the entire area, not localized to edges or isolated defects, suggesting that the dissolution results mainly from the permeation of water through the PBTPA film without other contributions.[16] Figure 4b shows that the water permeability and stable operation time (i.e., functional lifetime) can be controlled by the thickness of the PBTPA 1:4:7 encapsulation (here functional lifetime corresponds to the time over which resistance remains finite). A layer of PBTPA 1:4:7 with thickness of 100 μm exhibits water-barrier properties up to 13 h, while Mg resistor with PBTPA 1:4:7 with thickness of 600 μm can survive up to 95 h.

A 1D analytical model, detailed in the Experimental Section, captures the effects of reactive diffusion of PBS with the PBTPA encapsulation. The diffusivity estimated in this manner is $D_{PBPTA} = 0.97 \times 10^{-13}$ m^2 s^{-1}, which is close to the lower bound of reported diffusivity for biodegradable polymers.[28,29] In addition to spatially uniform dissolution of Mg, the results are consistent with water permeation through the PBTPA itself rather than by leakage at defect sites (a typical pathway in inorganic encapsulation layers[16]). This dependence on thickness and chemical composition of PBTPA can be used to control the timescales for diffusion-driven water penetration.

In certain cases, the thicknesses of the active materials can also be used to define the functional lifetime. Figure 4c shows measurements of changes in the resistance of Mg resistors with various thickness, encapsulated in PBTPA 1:4:7 with a thickness of 500 μm. Increasing the thickness of the Mg extends the time that the resistance remains below a certain threshold value. The case of a PBTPA encapsulated Mg resistor with thickness of ≈1.1 μm provides electrical continuity for more than 6 d. Figure 4d shows the relationship between Mg thickness and time. The linear relationship (5.4 d μm^{-1}) is consistent with surface erosion of the Mg.[30]

Figure 4e shows a simple bioresorbable device that uses a non-biodegradable light-emitting diode (LED), connected to an external power supply through PBTPA 1:4:7 (≈500 μm thick) encapsulated Mg strip electrodes (50 μm thickness; 300 μm width; 30 mm length). A PDMS well structure confines a volume of PBS (pH 7.4 at 37 °C) over the LED and the lines. The series of images in Figure 4e illustrate a gradual decrease in light emitted by the LED as a function of time of immersion. The intensity remains invariant for up to 50 d, consistent with measurements using the Mg resistor test structure, and begins to decrease rapidly through the 60th day until complete failure on the 70th day. A fully encapsulated bioresorbable device further confirms the effective water-barrier properties of PBTPA. Figure S15 (Supporting Information) shows the experimental setup and the design of bioresorbable wirelessly powered LED system, built with a biodegradable coil (Mg, width, 100 μm; thickness 50 μm), a biodegradable diode (Si nanomembrane active layer, 1.2 μm thick), and a non-biodegradable LED. The fabrication involves placing the bioresorbable electronic device on a partially cured layer of PBTPA and applying a liquid mixture of three chemical precursors (4PA, TTT, and BDT) on top. Illumination with UV completes the formation of PBTPA encapsulation on both the top and bottom sides of the system. Figure 4f shows photographs of during immersion in PBS (pH 7.4; 37 °C). The intensity of light emitted by the LED is maintained more than one month and decreases after 50 d, consistent with the results in Figure 4e. Figure S16 (Supporting Information) shows the mechanical flexibility of the system, illustrating robust operation during mechanical deformation. Replacing Mg with other more stable biodegradable metal foils, such as Mo, W, and Fe, further enhances the functional lifetime because the rate of dissolution of Mg (≈1 μm d^{-1} at 23 °C)[30] is much higher than that of Mo (20 nm d^{-1} at 23 °C), W (150 nm d^{-1} at 23 °C), and Fe (80 nm d^{-1} at 23 °C).[15,17]

2.5. Biocompatibility of PBTPA

In vivo biocompatibility of PBTPA is critically important for applications in bioresorbable implants. Inserting samples of PBTPA 1:4:7 and PLGA (65:35, FDA-approved nontoxic control)[31] subcutaneously into individual Balb/c mice yields data on foreign body reactions. The results in **Figure 5**a indicate that the changes in weight for mice with PLGA implants, as controls, and those with PBTPA implants mice are similar throughout the four weeks period of observation. Following implantation, the mice behave normally with no substantial skin necrosis or swelling for up to four weeks. Figure 5b shows the change in weight of major organs (kidney, liver, spleen, heart, lung, and brain) explanted from mice at two and four weeks after implantation, measured by inductively coupled plasma optical emission spectrometry (see the Experimental Section for sample preparation steps). The results indicate minimal differences, consistent with the absence of toxic effects. Hematoxylin and eosin (H&E) stained sections of implant sites surrounding tissues and major organs (brain, liver, kidney, spleen, lung, and heart) show comparable levels of immune cell infiltration between PLGA- and PBTPA-implanted tissues at day 14 (Figure 5c). Some minimal inflammatory responses and fibrosis appear in close proximity to the implants, but no significant evidence of injury or damage occurs at the adjacent tissue and muscle layers.

Quantitative data from histological studies provide further support for the biocompatibility of the material, as shown in Figure S17 (Supporting Information). Ten spots (area: 0.0625 mm^2) selected randomly from each organ show no significant differences between control (PLGA) and test (PBTPA) groups. Representative H&E images from the adjacent skin and heart tissues are in Figure S17a,c (Supporting Information), respectively. The counted immune cells (lymphocyte) from adjacent skin and heart tissues provide additional evidence of biocompatibility (Figure S17b,d, Supporting Information).

The results of complete blood chemistry tests provide a comprehensive understanding of the health of the mice (Figure 5d,e). Blood levels of enzymes and electrolytes, which serve as indicators of organ-specific diseases, fall within the confidence intervals of control values. For example, normal levels of alanine aminotransferase, cholesterol and triglyceride, phosphorus and urea nitrogen, calcium, albumin and total

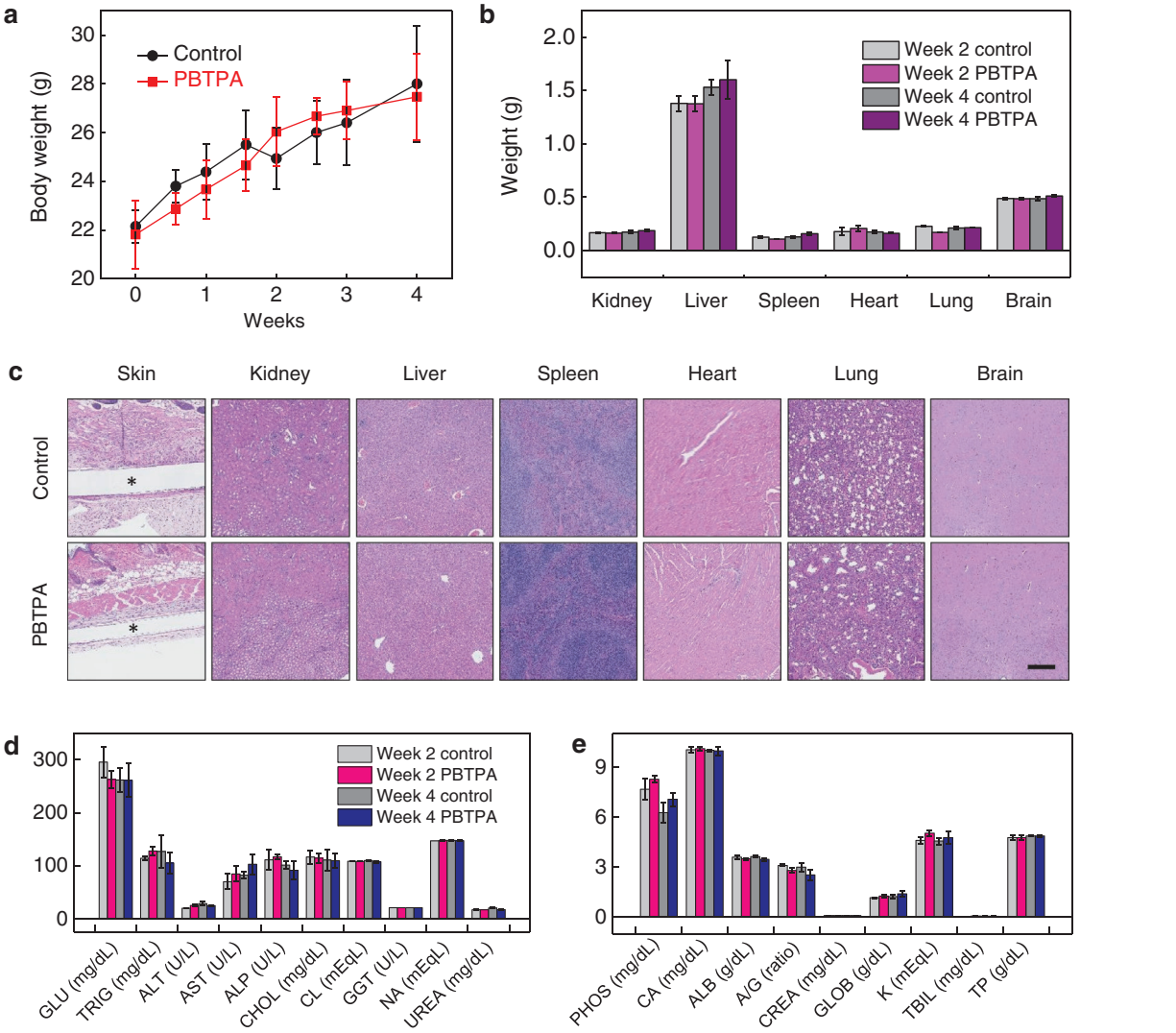

Figure 5. In vivo biocompatibility evaluation of PBTPA. a) Bodyweight in each group (control, $n = 6$; PBTPA, $n = 6$) measured weekly. b) Comparison of weight change of each organs at two weeks (control, $n = 3$; PBTPA, $n = 3$) and four weeks (control, $n = 3$; PBTPA, $n = 3$). c) Hemotoxylin and eosin-stained sections obtained in skin and major organs (brain, liver, kidney, spleen, lung, and heart) two-week postimplantation of PLGA (control group) and PBTPA (test group). Scale bar indicates 200 µm. $n = 3$ independent animals. d,e) Blood chemistry test for the groups ($n = 3$ per groups). ALP, alkaline phosphatase (IU L^{-1}); ALT, alanine aminotransferase (U L^{-1}); AST, aspartate transaminase (IU L^{-1}); CAL, calcium (mg dL^{-1}); CHOL, cholesterol (mg dL^{-1}); GLU, glucose (mg dL^{-1}); HCT, hematocrit level (%); HGB, blood hemoglobin level (g dL^{-1}); MCH, mean corpuscular hemoglobin (pg); MCV, mean corpuscular volume (fL); MPV, mean platelet volume (fL); PHOS, phosphorus (mg dL^{-1}); PLT, platelet count in blood (×1000 µL^{-1}); RBC, red blood cell (×1 000 000 µL^{-1}); RDW, red cell distribution width (%); TRIG, triglycerides (mg dL^{-1}); WBC, white blood cell (×1000 µL^{-1}). (All data presented as the average and standard error of mean (SEM).)

proteins indicate the absence of disorders in the liver, heart, kidney, bone and nerve, and good overall health, respectively.

3. Conclusion

The synthesis strategies, degradation kinetics, water absorption properties, water-permeability characteristics, and mechanical assessments summarized here provide guidelines for the chemical design of polyanhydride materials tailored for use as encapsulation layers and substrates in bioresorbable electronics. Demonstrations with partially bioresorbable LED circuits illustrate a simple application in this latter context. In vivo immunochemistry evidence suggests that these materials and their degradation products are biocompatible, indicating their potential for use in biomedical devices. The ability to change the rates of bioresorption through chemical modifications and thickness control provides access to a range of functional lifetimes, to meet application requirements. Increasing the percentage of BDT and/or the number of methylene groups between the two thiol terminations may lead to further increases in the lifetime.

4. Experimental Section

Synthesis of Polyanhydride: Cross-linking a mixture of 4PA, TTT, and BDT by illumination with UV light (intensity of 590 µW cm^{-2}; wavelength

of 365 nm) for 5 min with 2, 2-dimethoxy-2-phenylacetophenone as the photoinitiator (total mass of 0.5%) yielded a water-degradable PBTPA. All chemicals were purchased from Sigma Aldrich (USA). Three formulations of PBTPA were synthesized, defined by molar ratios 1:1:2.5, 1:2:4, and 1:4:7 of 4PA, TTT, and BDT, respectively. Silane (trichloro(1H, 1H, 2H, 2H-perfluorooctyl) silane) (Sigma Aldrich, USA) coated PDMS molds provide a way to control thickness of PBTPA film (100, 300, and 500 µm) by infiltration of the mixture of 4PA, TTT, and BDT.

Dissolution and Water Uptake Tests: Drop-casting the three different PBTPA formulations on glass slides and curing them by UV exposure for an hour formed ≈15 mm × 15 mm square samples. The initial average weights were 1.35 (±0.04), 1.29 (±0.05), and 1.31 (±0.03) g for PBTPA 1:1:2.5, PBTPA 1:2:4, and PBTPA 1:4:7, respectively. Immersing the samples into a 0.1 M phosphate buffered saline (Sigma-Aldrich, USA) with three different pH values (5.7, 7.4, and 8) at room temperature, removing the samples from the solutions at several different times, rinsing them with deionized (DI) water, drying the residual water under vacuum with P_2O_5 drying agent for 1 d, and weighing them yielded the hydrolysis kinetics. Comparison of the weights before and after drying under the vacuum provided the water uptake.

Water Permeability Test: Depositing Mg on a silicon dioxide (SiO_2) substrate by electron-beam (e-beam) evaporation through photolithographically patterned mask formed a water-soluble thin film resistor. Placing a layer of PBTPA 1:4:7 and a PDMS well filled with PBS 0.1 M on the Mg resistor yielded a platform for testing water permeation. Gold pads formed at the ends of the Mg resistors allowed measurements of the resistance. All circuit elements were encapsulated by PBTPA.

WVP Tests: Water vapor permeability was measured according to procedures similar to ASTM-E96. Briefly, a test chamber was maintained at 24 °C with 93% ± 5% relative humidity throughout test duration. Dry scintillation vials were filled with 10–12 g of desiccant prior to adhering the test specimen to the vial mouth with marine epoxy sealant. Test specimens were prepared in triplicate with average thicknesses between 100 and 200 µm. Vials with the attached polymer specimens were placed in the test chamber to begin the test. Weight measurements of the vials were recorded regularly on an analytical balance for a period of at least 10 d. Permeability values were determined using the following equation

$$\text{Permeability}\left(\text{g m m}^{-2}\,\text{h}^{-1}\,\text{Pa}^{-1}\right)=\left[\frac{\text{WVT}}{S(R_1-R_2)}\right]\cdot\text{thickness} \quad (3)$$

where WVT = $G/t{\cdot}A$ (G = weight change in grams, t = elapsed time at point of measurement, A = test area in m^2), S = saturation vapor pressure at test temperature (2986 Pa at 24 °C), R_1 = relative humidity of test chamber, R_2 = relative humidity at the vapor sink.

Fabrication and Dissolution Test of LED Circuit: Microscale electrodes of Mg (50 µm thickness) were fabricated by laser-cutting served as the conductive lines. A commercial LED (Digikey, USA) was interfaced to these lines by a conductive silver epoxy, mounted on a glass slide. The experiments involved placing a preformed film of PBTPA 1:4:7 (500 µm thickness) over the structure, and then applying a PDMS well filled PBS. The device setup was placed in an oven at 37 °C.

Water-Barrier Tests Using a Wireless Bioresorbable Device Fully Encapsulated with PBTPA: The fabrication involved placing the device on a partially cured (<1 min illumination of UV) layer of PBTPA and then applying a liquid mixture of three chemical precursors (4PA, TTT, and BDT). Subsequent illumination of UV (>5 min) completed the formation of an encapsulation on both top and bottom sides of the system. A transmission coil operated with a sine wave (amplitude = 5 V_{pp}) generated by a waveform generator (Agilent 33250A; Agilent Technologies) and placed underneath a glass reservoir that houses the system immersed in PBS (pH 7.4) provided power to support operation. This setup was placed in an oven at 37 °C, and the device operation was checked every 10 d by visually observing light emission from the LED.

In Vivo Biocompatibility Tests: Female CD1(8 weeks old) mice were purchased from Charles River Laboratories. All procedures were approved by the Institutional Animal Care and Use Committee of Northwestern University (protocol IS00005877). The mice were anesthetized with isoflurane gas (≈2%), PLGA (FDA-approved control), and samples of PBTPA were implanted subcutaneously through dorsal incision. Following 14 and 28 d of implantation, the mice were sacrificed for histology. Tissue samples were fixed in 10% neutral buffered formalin, embedded in paraffin, sectioned and stained with H&E for histological analysis. Lymphocytes were identified by morphology from ten distinct regions by 400 × fields per sample. Histological scores were assessed as reported earlier.[32] Ten random locations were chosen for the capsule thickness measurements from optical microscopy images at 10× magnification.[32]

Modeling of Reactive Diffusion for Polyanhydride Encapsulated Mg: A 1D analytical model can be used to describe the reaction and diffusion processes of a single Mg layer and PBTPA encapsulated Mg while immersed in an aqueous solution (PBS at pH 7.4, 37 °C). The model, adopted from Li et al.[33] and used in Won et al.[28] for natural wax, applies since the single Mg layer thickness (h_0) and the polyanhydride/Mg specimen thickness ($h_0 + h_{PBTPA}$), where h_0 and h_{PBTPA} are the initial thicknesses of the Mg layer and PBTPA encapsulation, respectively, is much smaller compared to its diameter (Note S1, Supporting Information). The resistance of Mg is given by $R=\frac{R_0 h_0}{h}$ where R_0 is the initial resistance. Using the equation for normalized Mg thickness (Equation (S12) in Note S1, Supporting Information), the critical time t_c (i.e., functional lifetime) can be determined for the resistance to reach a critical value (i.e., R = 500 Ω) by using $R_0 \approx$ 37 Ω, measured from experiments, and setting $\frac{h(t_c)}{h_0}=0.075$. For a single Mg layer, the normalized thickness and the critical time are given by Equations (S14) and (S15) in Note S1 (Supporting Information). The material parameters used in the single Mg layer and PBTPA encapsulation model are given in Li et al.[33] and Won et al.[28] as M_{Mg} = 24 g mol $^{-1}$, M_{H_2O} = 18 g mol $^{-1}$, ρ_{Mg} = 1.738 g cm^{-3}, w_0 = 1 g cm^{-3}, $k = 1.2\times10^{-3}$ s^{-1}, and $D = 6.0\times10^{-16}$ m^2 s^{-1}. The parameter D_{PBTPA} was obtained by fitting the experimental data as shown in Figure 4b for PBTPA (0.97×10^{-13} m^2 s^{-1}).

Evaluations of Blood Chemistry: Autoclave sterilized samples of PBTPA and PLGA were implanted in the back subdermal regions of the mice. The procedures involved anaesthetizing a female CD-1 mouse (Charles River Laboratories) with isoflurane gas (≈2%), opening a 1-cm-length pocket at the subcutaneous region near the right flank, inserting the device into the pocket, and suturing to close the surgical opening. The procedures were approved by the Institutional Animal Care and Use Committee of Northwestern University (protocol IS00005877). Daily checking, weighing, and care of the mice ensured their moribund conditions and normal stress exposure. Euthanasia of three mice at two and four weeks after device implantation, blood extraction, dissection, and weighing of major organs, including the brain, heart, kidney, liver, lung, muscle, and spleen. Charles River Laboratories conducted complete blood chemistry tests on the blood samples collected in K-EDTA tubes and gel tubes, respectively.

Supporting Information

Supporting Information is available from the Wiley Online Library or from the author.

Acknowledgements

Y.S.C. and J.K. contributed equally to this work. This work made use of the NUFAB facility of Northwestern University's NUANCE Center, which has received support from the Soft and Hybrid Nanotechnology Experimental (SHyNE) Resource (NSF ECCS-1542205); the MRSEC program (NSF DMR-1720139) at the Materials Research Center; the Querrey-Simpson Institute for Bioelectronics; the Keck Foundation; and the State of Illinois, through the IIN. J.K. acknowledges the support from Korea University (Grant No. K2008831) R.A. acknowledges support from the National Science Foundation Graduate Research Fellowship (NSF

Grant No. 1842165) and Ford Foundation Predoctoral Fellowship. S.K.K. was supported by the National Research Foundation of Korea (NRF) grant funded by the Korea government (MSIT) (NRF-2019R1C1C1004232) and by KIST Institutional Program (Project No. 2V07080-19-P141). J.Kim, K.L, and K.Lee were supported by NRF-2018M3A9D3079285.

Conflict of Interest

The authors declare no conflict of interest.

Keywords

biodegradable polymer, bioresorbable polymer, biocompatible polymer, encapsulation, hydrophobic polymer, transient electronics

Received: January 31, 2020
Revised: March 30, 2020
Published online: June 9, 2020

[1] A. L. Chamis, G. E. Peterson, C. H. Cabell, G. R. Corey, R. A. Sorrentino, R. A. Greenfield, T. Ryan, L. B. Reller, V. G. Fowler, *Circulation* **2001**, *104*, 1029.
[2] L. Hall-Stoodley, J. W. Costerton, P. Stoodley, *Nat. Rev. Microbiol.* **2004**, *2*, 95.
[3] C. M. Boutry, H. Chandrahalim, P. Streit, M. Schinhammer, A. C. Hänzi, C. Hierold, *Philos. Trans. R. Soc., A* **2012**, *370*, 2418.
[4] M. Maytin, L. M. Epstein, *Circ.: Arrhythmia Electrophysiol.* **2010**, *3*, 413.
[5] K. Ott, E. Tarlov, R. Crowell, N. Papadakis, *J. Neurosurg.* **1976**, *44*, 80.
[6] G. V. Vajramani, G. Jones, R. Bayston, W. P. Gray, *Br. J. Neurosurg.* **2005**, *19*, 496.
[7] J. Shin, Y. Yan, W. Bai, Y. Xue, P. Gamble, L. Tian, I. Kandela, C. R. Haney, W. Spees, Y. K. Y. Lee, M. Choi, J. Ko, H. Ryu, J. K. Chang, M. Pezhouh, S. K. Kang, S. M. Won, K. J. Yu, J. Zhao, Y. K. Y. Lee, M. R. MacEwan, S. K. Song, Y. Huang, W. Z. Ray, J. A. Rogers, *Nat. Biomed. Eng.* **2019**, *3*, 37.
[8] S. K. Kang, R. K. J. Murphy, S. W. Hwang, S. M. S. H. Lee, D. V. Harburg, N. A. Krueger, J. Shin, P. Gamble, H. Cheng, S. Yu, Z. Liu, J. G. McCall, M. Stephen, H. Ying, J. Kim, G. Park, R. C. Webb, C. H. Lee, S. Chung, D. S. Wie, A. D. Gujar, B. Vemulapalli, A. H. Kim, K. M. Lee, J. Cheng, Y. Huang, S. M. S. H. Lee, P. V. Braun, W. Z. Ray, J. A. Rogers, *Nature* **2016**, *530*, 71.
[9] S. W. Hwang, C. H. Lee, H. Cheng, J. W. Jeong, S. K. Kang, J. H. Kim, J. Shin, J. Yang, Z. Liu, G. A. Ameer, Y. Huang, J. A. Rogers, *Nano Lett.* **2015**, *15*, 2801.
[10] W. Bai, J. Shin, R. Fu, I. Kandela, D. Lu, X. Ni, Y. Park, Z. Liu, T. Hang, D. Wu, Y. Liu, C. R. Haney, I. Stepien, Q. Yang, J. Zhao, K. R. Nandoliya, H. Zhang, X. Sheng, L. Yin, K. MacRenaris, A. Brikha, F. Aird, M. Pezhouh, J. Hornick, W. Zhou, J. A. Rogers, *Nat. Biomed. Eng.* **2019**, *3*, 644.
[11] J. Koo, M. R. MacEwan, S.-K. K. Kang, S. M. Won, M. Stephen, P. Gamble, Z. Xie, Y. Yan, Y.-Y. Y. Chen, J. Shin, N. Birenbaum, S. Chung, S. B. Kim, J. Khalifeh, D. V. Harburg, K. Bean, M. Paskett, J. Kim, Z. S. Zohny, S. M. Lee, R. Zhang, K. Luo, B. Ji, A. Banks, H. M. Lee, Y. Huang, W. Z. Ray, J. A. Rogers, *Nat. Med.* **2018**, *24*, 1830.
[12] C. H. Lee, S. K. Kang, G. A. Salvatore, Y. Ma, B. H. Kim, Y. Jiang, J. S. Kim, L. Yan, D. S. Wie, A. Banks, S. J. Oh, X. Feng, Y. Huang, G. Troester, J. A. Rogers, *Adv. Funct. Mater.* **2015**, *25*, 5100.
[13] H. Tao, S. W. Hwang, B. Marelli, B. An, J. E. Moreau, M. Yang, M. A. Brenckle, S. Kim, D. L. Kaplan, J. A. Rogers, F. G. Omenetto, *Proc. Natl. Acad. Sci. USA* **2014**, *111*, 17385.
[14] S.-W. Hwang, H. Tao, D.-H. Kim, H. Cheng, J.-K. Song, E. Rill, M. A. Brenckle, B. Panilaitis, S. M. Won, Y.-S. Kim, Y. M. Song, K. J. Yu, A. Ameen, R. Li, Y. Su, M. Yang, D. L. Kaplan, M. R. Zakin, M. J. Slepian, Y. Huang, F. G. Omenetto, J. A. Rogers, *Science* **2012**, *337*, 1640.
[15] Y. S. Choi, J. Koo, J. A. Rogers, *MRS Bull.* **2020**, *45*, 103.
[16] S. K. Kang, S. W. Hwang, H. Cheng, S. Yu, B. H. Kim, J. H. Kim, Y. Huang, J. A. Rogers, *Adv. Funct. Mater.* **2014**, *24*, 4427.
[17] S. K. Kang, S. W. Hwang, S. Yu, J. H. Seo, E. A. Corbin, J. Shin, D. S. Wie, R. Bashir, Z. Ma, J. A. Rogers, *Adv. Funct. Mater.* **2015**, *25*, 1789.
[18] W. M. Grill, S. E. Norman, R. V. Bellamkonda, *Annu. Rev. Biomed. Eng.* **2009**, *11*, 1.
[19] E. S. Place, J. H. George, C. K. Williams, M. M. Stevens, *Chem. Soc. Rev.* **2009**, *38*, 1139.
[20] R. Ghadi, E. Muntimadugu, A. J. Domb, W. Khan, X. Zhang, *Synthetic Biodegradable Medical Polymer: Polyanhydrides*, Elsevier, Amsterdam **2017**.
[21] A. Basu, A. J. Domb, *Adv. Mater.* **2018**, *30*, 1706815.
[22] A. Gopferich, J. Tessmar, *Adv. Drug Delivery Rev.* **2002**, *54*, 911.
[23] L. Erdmann, K. E. Uhrich, *Biomaterials* **2000**, *21*, 1941.
[24] F. Fallegger, G. Schiavone, S. P. Lacour, *Adv. Mater.* **2019**, 1903904.
[25] D. R. Enzmann, N. J. Pelc, *Radiology* **1992**, *185*, 653.
[26] M. Carlsson, P. Cain, C. Holmqvist, F. Stahlberg, S. Lundback, H. Arheden, *Am. J. Physiol.: Heart Circ. Physiol.* **2004**, *287*, H243.
[27] D. E. Harrison, R. Cailliet, D. D. Harrison, S. J. Troyanovich, S. O. Harrison, *J. Manipulative Physiol. Ther.* **1999**, *22*, 227.
[28] S. M. Won, J. Koo, K. E. Crawford, A. D. Mickle, Y. Xue, S. Min, L. A. McIlvried, Y. Yan, S. B. Kim, S. M. Lee, B. H. Kim, H. Jang, M. R. MacEwan, Y. Huang, R. W. Gereau, J. A. Rogers, R. W. GereauIV, J. A. Rogers, R. W. Gereau, J. A. Rogers, *Adv. Funct. Mater.* **2018**, *28*, 1801819.
[29] J.-S. Yoon, H.-W. Jung, M.-N. Kim, E.-S. Park, *J. Appl. Polym. Sci.* **2000**, *77*, 1716.
[30] L. Yin, H. Cheng, S. Mao, R. Haasch, Y. Liu, X. Xie, S. W. Hwang, H. Jain, S. K. Kang, Y. Su, R. Li, Y. Huang, J. A. Rogers, *Adv. Funct. Mater.* **2014**, *24*, 645.
[31] S. Lee, J. Koo, S. K. Kang, G. Park, Y. J. Lee, Y. Y. Chen, S. A. Lim, K. M. Lee, J. A. Rogers, *Mater. Today* **2018**, *21*, 207.
[32] G. Park, H. J. Chung, K. Kim, S. A. Lim, J. Kim, Y. S. Kim, Y. Liu, W. H. Yeo, R. H. Kim, S. S. Kim, J. S. Kim, Y. H. Jung, T. I. Kim, C. Yee, J. A. Rogers, K. M. Lee, *Adv. Healthcare Mater.* **2014**, *3*, 515.
[33] R. Li, H. Cheng, Y. Su, S. W. Hwang, L. Yin, H. Tao, M. A. Brenckle, D. H. Kim, F. G. Omenetto, J. A. Rogers, Y. Huang, *Adv. Funct. Mater.* **2013**, *23*, 3106.

